Structural-Fluidic-Acoustic Computational Modelling and Experimental Validation of Piezoelectric Synthetic Jet Actuators

Gungordu B.[a,*], Jabbal M.[b], Popov A.A.[b]

[a] *Aerospace Engineering, Middle East Technical University, Northern Cyprus Campus, Guzelyurt via Mersin 10, 99738 Kalkanli, Turkey*
[b] *Faculty of Engineering, University of Nottingham, Nottingham, NG7 2RD, UK*

Abstract

In this study, coupled structural-fluidic-acoustic modelling of piezoelectric diaphragm driven synthetic jet actuators is conducted computationally for the first time. The aim is to demonstrate the importance of piezoelectric diaphragm structural modelling and the effects of acoustics coupling to compute accurate synthetic jet exit jet velocity. Two different synthetic jet actuator orifice-diaphragm configurations are studied in which the orifice is parallel and adjacent to the diaphragm, namely, opposite and adjacent synthetic jet actuators, respectively. In investigating the aforementioned configurations, cavity acoustic and mechanical resonance frequencies are identified within ± 100 Hz, compared to in-house experimental measurements of laser vibrometry and hot-wire anemometry. The numerical peak jet velocity differs from the experimental value at the diaphragm mechanical resonance by 5.4% and 0.3% for opposite and adjacent synthetic jets, respectively. Further analysis of velocity and vorticity fields showed that no vortex formation is observed in the cavity of the adjacent synthetic jets, despite having similar exit jet velocity of the opposite synthetic jet configuration.

Keywords: Synthetic jets, CFD, Modelling, Coupling

*Corresponding author
Email address: barisgungordu@hotmail.com (Gungordu B.)

Nomenclature

c	=	Speed of sound (ms^{-1})
d_o	=	Orifice diameter (mm)
d_{31}	=	Transverse piezoelectric coefficient (pm/V)
D_{brass}	=	Brass substrate diameter (mm)
D_{pzt}	=	Piezoelectric patch diameter (mm)
D_c	=	Cavity diameter (mm)
f	=	Actuation frequency (Hz)
f_H	=	Helmholtz resonance frequency (Hz)
f_M	=	Mechanical resonance frequency (Hz)
h	=	Orifice neck height (mm)
H	=	Cavity height (mm)
L	=	Stroke length (mm)
r_{brass}	=	Brass substrate radius (mm)
r_{pzt}	=	Piezoelectric patch radius (mm)
Re_{U_p}	=	Reynolds number (-)
S	=	Stokes number (-)
St	=	Strouhal number (-)
t_{brass}	=	Thickness of brass substrate (mm)
t_{pzt}	=	Thickness of piezoelectric patch (mm)
T	=	Period of oscillation (s)
U_p	=	Mean peak jet velocity (ms^{-1})
$\mathbf{v}$	=	Velocity field (ms^{-1})
V_p	=	Peak supply voltage (V)
μ	=	Dynamic viscosity (Pa.s)
μ_B	=	Bulk viscosity (Pa.s)
ϕ	=	Phase angle difference (rad)
ρ	=	Density (kg m^{-3})
ζ	=	Material damping ratio (-)

1. Introduction

A synthetic jet actuator (SJA) is a zero-net-mass-flux device which essentially works like a Helmholtz resonator and consists of an actuator (i.e., piston [1, 2], loudspeaker [3, 4], or piezoelectric diaphragm [5, 6]), cavity, and orifice plate [7]. The actuator energizes still fluid in the cavity, which starts discharging through the orifice. If the synthetic jet formation criterion is met, counter-rotating vortex rings form close to the orifice exit [8, 9, 10]. SJAs have been proposed for various applications, including flow separation control [11], thrust vectoring [12], mixing enhancement [13], and electronic equipment cooling [14].

The SJA is a challenging electro-mechanical-fluidic device from a modelling point of view due to the involvement of multiphysical domains (structural, acoustic, fluidic) and geometric (actuator size, diaphragm composition), and operational parameters (actuation voltage, and frequency) that motivate the need to have reliable modelling tools to minimise experimental testing time. High fidelity modelling of the isolated (i.e., on-bench) actuator would help improve understanding of the SJA, which would lead the focus of research towards implementing the actuator to an engineering application such as separation/circulation control of aerofoils [15, 16].

There has been a wealth of research in the numerical investigation of SJA in different configurations (i.e., opposite & adjacent synthetic jets) and amplification mechanisms. Numerical efforts to date can be classified into three groups such as computational fluid dynamics (CFD) studies [17, 18, 19, 20], Lumped Element Models [21, 22, 23] and fluidic-acoustic analytical [24, 25, 26] (also referred to as Runge-Kutta type [27]) models.

In previous numerical studies, the SJA was commonly modelled using CFD simulations, where Navier-Stokes equations are solved numerically. The main advantage of computational modelling is obtaining state variables (i.e., flow velocity, pressure, density) at any point in the geometry and flow visualisation. Experimental flow visualisation techniques are challenging for SJA. This is because it is difficult to get measurements to understand the flow physics inside the

cavity. Therefore, CFD simulation should be used for more detailed quantitative and qualitative understanding of the SJA internal flow.

Figure 1 illustrates SJA jet velocity response and also presents the cavity acoustic (i.e., Helmholtz, f_H) and diaphragm mechanical resonance frequency (f_M). The experiment is taken from Gallas et al. [28]. The acoustic simulation marker in Figure 1 is obtained from a simulation of SJA with only the Helmholtz equation, with a displacement boundary condition to replace the piezoelectric diaphragm. This type of simulation yields the frequency response of a Helmholtz resonator. The fluidic simulation marker in the figure is a CFD of the piezoelectric diaphragm with the RANS k-omega turbulence closure model. The breakthrough of the fluidic model is the combination of the structural model of the piezoelectric diaphragm and the fluidic simulation which yields accurate resonance frequency and diaphragm displacement computations. Even though this type of simulation can identify the jet velocity increase due to the diaphragm's mechanical resonance, the velocity enhancement due to the acoustic resonance cannot be captured. Moreover, the coupling of the two resonances, observed experimentally, cannot be obtained. Therefore, a hybrid mathematical model which can capture the structural, acoustic, and fluidic response of a SJA is required.

Table 1 shows key results from selected CFD studies, including experimental validation. It consider the size of the orifice (or slot), cavity diameter, actuation frequency, and piezoelectric diaphragm model (or boundary condition, abbreviated as B.C.), and the accuracy which is the percentage difference with the experimental data at peak exit jet velocity. PZT-diaphragm in Table 1 stands for a study with a structural piezoelectric diaphragm modelling.

The following conclusions can be drawn by analyzing Table 1, which identifies the research gaps:

- Structural mechanics of the diaphragm is often not modelled and replicated with a sinusoidal boundary condition.
- No such computational model can obtain jet velocity response correspond-

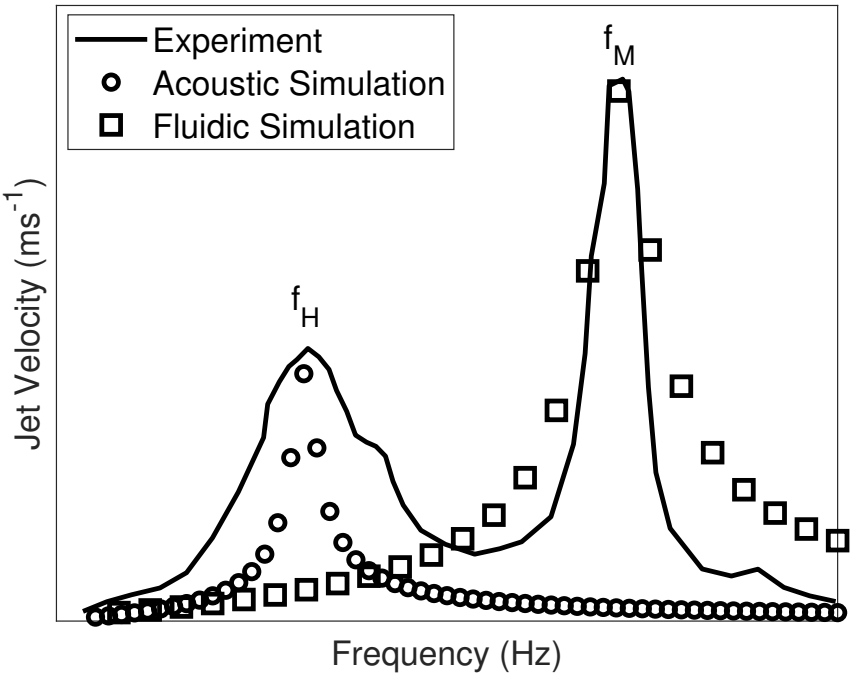

Figure 1: Jet Velocity Frequency Response of SJA according to Gallas et al. [28]

Table 1: Review of synthetic jet actuator CFD Studies (B.C. 1 = Velocity boundary condition at the orifice exit plane, B.C. 2 = Moving membrane modelled by an equation, B.C. 3 = Moving piston condition)

Study	d_o (mm)	D_c (mm)	f (Hz)	Model	Accuracy (%)
[17]	0.5 x 75	N/A	1000	B.C. 1	10
[29]	0.5 x 75	15	1000	B.C. 1	N/A
[30]	0.75	36.8	1450	B.C. 1	50
[31]	5	45	50	B.C. 2	10
[18]	3	45	200-1100	B.C. 2	28
[19]	1.65 x 9.6	75	57	B.C. 3	10
[20]	2	30.8	199	B.C. 3	16.5
[32]	3	40	20	PZT-diaphragm	15

ing to the cavity acoustic resonance (i.e., Helmholtz) and the diaphragm mechanical resonance, due to the lack of coupled structural-fluidic-acoustic models.

- Further improvement is required to reduce the experimental and computational jet velocity difference.

- To avoid resonance contamination, in most cases, very low actuation frequency is studied, which does not have much significance on SJA sizing, development, and industrial relevance.

The main implication of numerically solving Navier-Stokes equations with the continuity equation and a turbulence model (if the flow is not laminar) is omitting the acoustics aspects of the actuator. Thus, Helmholtz resonance and associated effects on the jet velocity cannot be obtained.

The current study aims to develop a computational model of the SJA which can capture both resonance frequency and validate it against in-house experimental data via the most significant performance metrics, such as diaphragm displacement and exit jet velocity. The simulations are conducted and compared with two different SJA configurations: opposite and adjacent orifice-diaphragm configurations driven by a common piezoelectric diaphragm. Additionally, the investigation analyses the velocity and vorticity field of the SJA in the orifice near-field region.

The objectives of the current study are to:

- Model the piezoelectric diaphragm to study the full spectrum of actuation frequencies

- Account for the pressure acoustics required to capture the cavity acoustic (i.e., Helmholtz) resonance

- Model high-frequency actuation to get the full frequency response function of the diaphragm displacement and output jet velocity

- Capture flow visualizations inside and outside of the SJA at the mechanical resonance frequency
- Study high exit jet velocity without significant model modification

2. Numerical Methods

This section presents the adopted numerical methods and explains the details of the computational work.

2.1. Mathematical Model

In this paper, synthetic jet actuators are studied numerically using a commercial CFD solver, COMSOL Multiphysics (version 5.3a) which employs finite element methods for the discretization of the equations [33]. The circular piezoelectric actuator consists of a single layer of substrate (herein brass) and piezoceramic layer (herein PZT-5A), which is commonly used in the literature [6, 34, 35]. The piezoelectric diaphragm is modeled using the inverse piezoelectric effect, which directly inputs force exerted by the diaphragm to the cavity fluid medium, as a pressure boundary condition.

Solid mechanics and electrostatics modules are employed to mimic the structural mechanics of the plates and the voltage applied to the piezoceramic plate, respectively. Two physics interfaces are coupled to reflect the inverse piezoelectric effect. The equations behind the simulation use standard piezoelectric stress-strain relationships and linear deflection equations under force ($\mathbf{F}$). The force is due to the voltage applied to the piezoceramic layer, and $\mathbf{u}$ is the displacement vector [33].

$$-\rho\omega^2\mathbf{u} = \nabla.s + \mathbf{F}\nu e^{i\phi} \tag{1}$$

The strain tensor (s) is computed by the following equation where the $\mathbf{c}_e$ is the elasticity matrix, and ϵ is the strain displacement of the piezoelectric patch. Electrical field ($\mathbf{E}$) and e^T are the piezoelectric constant that relates the stress applied to the mechanical strain [33].

$$s = s_0 + \mathbf{c}_e : \epsilon_e l - \mathbf{e}^T \mathbf{E} \tag{2}$$

The strain is calculated by the following equation:

$$\epsilon = \frac{1}{2}(\nabla \mathbf{u}^T + \nabla \mathbf{u}) \tag{3}$$

The mechanical damping is modelled as an isotropic structural loss factor in the elasticity matrix ($\mathbf{c}_e$). The elasticity matrix is multiplied with a loss factor (η_s) of $1 + i\eta_s$ [33].

$$\mathbf{c_e} = (1 + i\eta_s)\mathbf{c_e} \tag{4}$$

The only empirical term in the numerical model is the material damping ratio associated with the diaphragm. Nevertheless, true mechanical damping values obtained from the experiments are used in this study. Empirical damping extraction is beyond the scope of the current study.

The diaphragm is fixed at the edges where the displacement vector $\mathbf{u}$ is set to zero, which is the boundary condition matching the experiment. Considering the central symmetry, Figure 2 illustrates the clamping condition of the piezoelectric diaphragm. Triangular mesh elements are used with a maximum size of 0.0135 mm and a minimum size of 0.00027 mm. The total number of mesh elements on the plates is 19364. The mesh convergence is checked, and the mesh does not have a significant effect on the mechanical resonance frequency, ± 1 Hz. A pressure boundary condition, p(r,t), is applied on the top of the diaphragm to get the pressure raised by the diaphragm along the radius in the time domain.

The wave equation for acoustic waves reduces to an inhomogeneous Helmholtz equation.

$$\frac{1}{\rho c^2}\frac{\partial^2 p}{\partial t^2} - d_{\mathrm{a}}\frac{\partial p}{\partial t} + \nabla \cdot \left(-\frac{1}{\rho}\left(\nabla p - \mathbf{q}_d\right)\right) = Q_m \tag{5}$$

In Equation (5), Q_m term is the monopole domain source (radiates sound isotropically equally in all directions) and q_d is the dipole domain source (does

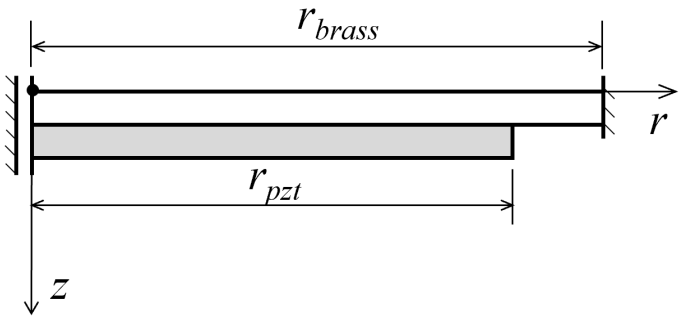

Figure 2: Illustration of the clamping conditions of the piezoelectric diaphragm, considering the central symmetry

not radiate sound isotropically) and p is the pressure. A loss term as a damping coefficient (d_a) is used as a first-order time derivative [33].

For compressible flow, a full set of linearised Navier-Stokes equations (Eq. 6) are solved together with the continuity equation (Eq. 7).

$$\rho \frac{\partial \mathbf{v}}{\partial t} = \nabla \cdot \left[-p\mathbf{I} + \mu \left(\nabla \mathbf{v} + (\nabla \mathbf{v})^T \right) - \left(\frac{2}{3}\mu - \mu_B \right) (\nabla \cdot \mathbf{v}) \, \mathbf{I} \right] \tag{6}$$

$$\frac{\partial \rho}{\partial t} + (\nabla \cdot \rho \mathbf{v}) = 0 \tag{7}$$

Where $\mathbf{v}$ is the fluid velocity and ρ is fluid density. Equations (6-7) are used at the orifice neck and near surroundings where the effects of viscosity dominate the flow characteristics. The effects of turbulence are simulated by an eddy viscosity (μ) and bulk viscosity (μ_B). The eddy viscosity approach for the turbulence closure problem is proven to be effective for oscillatory jets [36].

The pressure arises from the motion of the diaphragm coupled with the pressure acoustics in the cavity, which finally couples with thermo-viscous acoustic flow physics in the proximity of the orifice neck. Essentially, this creates a three-way coupled set of equations that properly models the structural-fluidic-acoustic foundations of synthetic jet actuators.

2.2. Geometry, Meshing and Time Domain Study

The SJA models are 3-D and shown in Figures 3a-3b, which illustratively introduce the geometry. The piezoelectric diaphragm is modeled as two stack layer of substrate and piezoceramic patch. The cavity and orifice walls are hard walls acoustically, and the no-slip condition is prescribed. The diaphragm motion inputs a boundary pressure load which turns into pressure fluctuations at the cavity and gives rise to the fluid movement towards the outer domain via the orifice neck.

The outer domain is used for flow visualization and represents the quiescent conditions, such as no pressure gradient is present in the outer space. Its dimensions are $20 \times d_o$ in the direction of the flow (z-axis) and $20 \times d_o$ in the lateral direction (y-axis). This is sufficient to avoid effects on the resulting jet and to ensure domain size independence of results [18]. The mesh is denser in the cavity and orifice neck, where viscosity plays an important role, and less dense in the outer domain. Also, it is known that orifice neck and exit regions are the most sensitive regions of the domain to the grid size and may affect computation [18].

Two configurations are studied within the computational modelling of the actuator. Figure 3a shows the geometry and meshing for the opposite diaphragm-orifice configuration actuator with an exploded view of the mesh in the orifice neck region. Figure 3b shows the geometry and an example meshing with an exploded view of the orifice neck for the adjacent orifice-diaphragm configuration actuator.

Table 2 shows results for jet velocities and the difference between three meshes applied with different mesh densities. Mesh convergence is checked and ensured it has minimal effect on the computations. Fine mesh is selected and used throughout the study. On top of the standard triangular and tetrahedral mesh, a boundary layer mesh is also employed at the orifice neck for finer resolution at the walls, which critically impacts the near-field computations [18, 37]. The boundary layer mesh consists of layered prism mesh elements with denser distribution, and it ensures at least 100 mesh elements are inside the oscillating

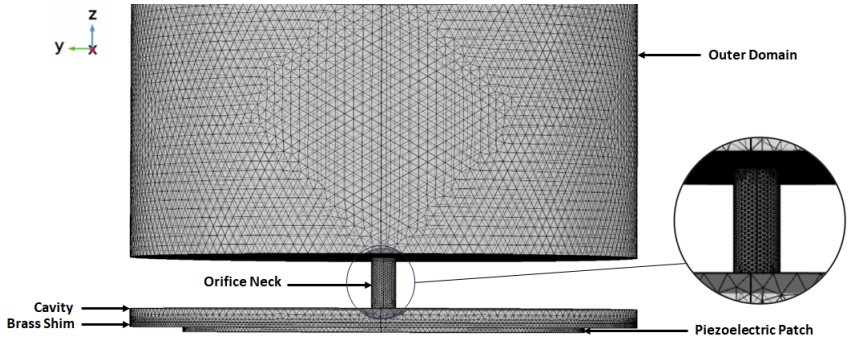

(a)

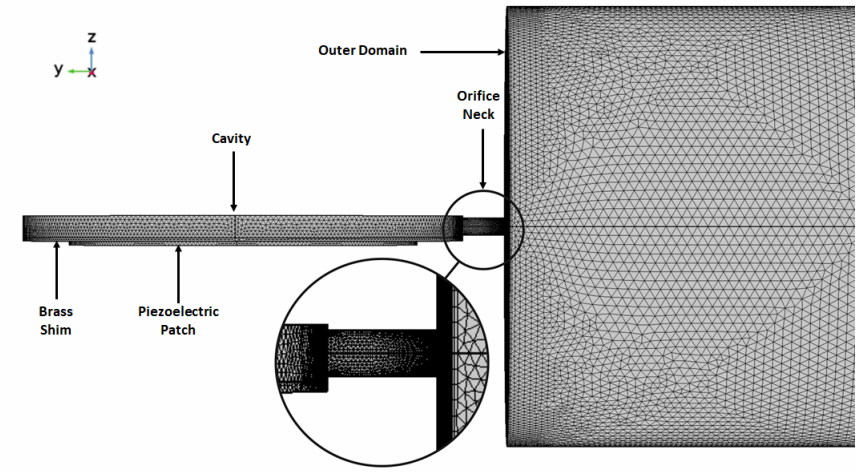

(b)

Figure 3: Geometry and meshing for orifice-diaphragm configurations (a) opposite (b) adjacent

boundary layer along the orifice length.

Table 2: Simulation mesh convergence test

Mesh	Coarse	Medium	Fine
Number of Nodes	637150	1318389	3543262
Boundary Elements	178512	265604	388038
Jet Velocity (ms^{-1})	37.99	37.29	36.81

For the transient study, each forcing frequency is studied for at least 100

cycles/periods (T = 1/f) to ensure a steady state, with $1/(2000f)$ time steps for each period which is found effective to capture both positive and negative peaks similar to the study by Jain et al. [18]. The computational jet velocity are collected by using spatial probes, which record the data at every time step and are located at the two ends of the orifice for spatial averaging. The first ten actuation cycles are discarded to ensure a steady state to avoid variations, and at consecutive peaks do not have a mathematically significant difference; less than 0.1%.

3. Experimental setup and methods

This section presents experimental methods for measuring diaphragm displacement and jet velocity.

The center position of the circular diaphragm is targeted, as it is one of the key piezoelectric performance indicators and is linked to the exit jet velocity in many studies, see e.g. [22, 38]. The laser scanning head used is a PSV-300 (Polytec). The laser measurements concentrated on identifying the resonant frequency and peak displacement at the center of the diaphragm. The laser controller was integrated into a dynamic signal generator and analyzer (Stanford Research SR-785). Sinusoidal excitation with a range of frequencies was used for all the tests conducted. The signal was amplified using a Trek Piezo Driver/Power Amplifier Model PZD350. Throughout the experiments, the input voltage amplitude was kept constant at 20 V_p.

Displacement measurements are taken in mm/s/V, which are then integrated with post-processing to obtain the peak displacement. The measurements are taken with a sampling rate of 40 kHz, which grant the Nyquist sampling criteria since the maximum actuation frequency is 4 kHz [39]. The resolution of the measurements is 5 μm/s. The displacement amplitude error at room temperature is $\pm$1.5% of the root-mean-square of the reading.

The real-time data acquired by using an analog-to-digital converter (NI cDAQ-9171) is connected to the computer (i.e., data acquisition software).

Hot-wire anemometry (HWA), MiniCTA 54T30 (Dantec Dynamics), is used for the jet velocity measurements with a 55P11 probe. The probe is positioned in line with the orifice center-line throughout the experiments as illustrated in Figure 4. Dantec 55P11 probe consists of a platinum-plated tungsten wire with a width of 1.2 mm (which is equal to or smaller than d_o) and a diameter of 5 μm. The position of the probe is set manually using a digital vernier caliper with a resolution of ± 0.05 mm.

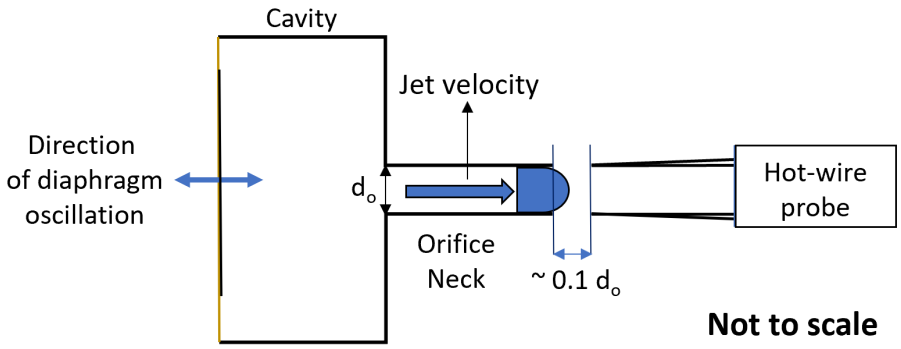

Figure 4: Illustration of hot-wire probe positioning and setup

Hot-wire calibration uses a nozzle rig, standard K-type thermocouples to measure flow temperature, and a Furness Control FC-0510 micro-manometer. The hot-wire probe is calibrated up to a 150 ms^{-1} velocity, and the calibration curve is fitted to a 5^{th} order polynomial. The sampling frequency and sample size are 10 kHz (satisfies Nyquist sampling criteria) and 100,000 for each forcing frequency. The measurements are corrected for temperature drift. The equipment accuracy of the hot-wire system and the calibration and positioning error is 3%.

4. Validation of the numerical model

In this section, the diaphragm displacement and exit jet velocity results of the numerical model are compared with the in-house experimental data. The actuator in validation Case 1 is an opposite orifice-diaphragm configuration (see

Figure 3a), and in validation Case 2, an adjacent orifice-diaphragm configuration is used (see Figure 3b). In both configurations, a common piezoelectric diaphragm is used, and its size and composition are presented in Table 3. The orifice and cavity size are optimized to maximise the exit jet velocity for both configurations [5, 40].

Table 3: Piezoelectric diaphragm size, piezoelectric coupling coefficient, and diaphragm material damping ratio (ζ)

Parameter	**Value**
D_{brass} (mm)	27
D_{pzt} (mm)	19.8
t_{brass} (mm)	0.22
t_{pzt} (mm)	0.23
d_{31} (m/V)	-180 x 10^{-12}
ζ (-)	0.0324

Figure 5 shows the positions of the diaphragm where flow visualizations of the actuator geometry are presented. Four positions are selected where the diaphragm is at peak expulsion ($\pi/2$), neutral position (π), peak suction ($-\pi/2$), and a quarter cycle away from the peak blowing ($-\pi/4$).

4.1. Validation Case 1

Table 4 introduces the diaphragm and actuator size for validation Case 1.

Table 4: Validation Case 1 - Cavity and orifice dimensions

Parameter	**Value**
d_o (mm)	1.0
D_c (mm)	25
h (mm)	2.5
H (mm)	0.67

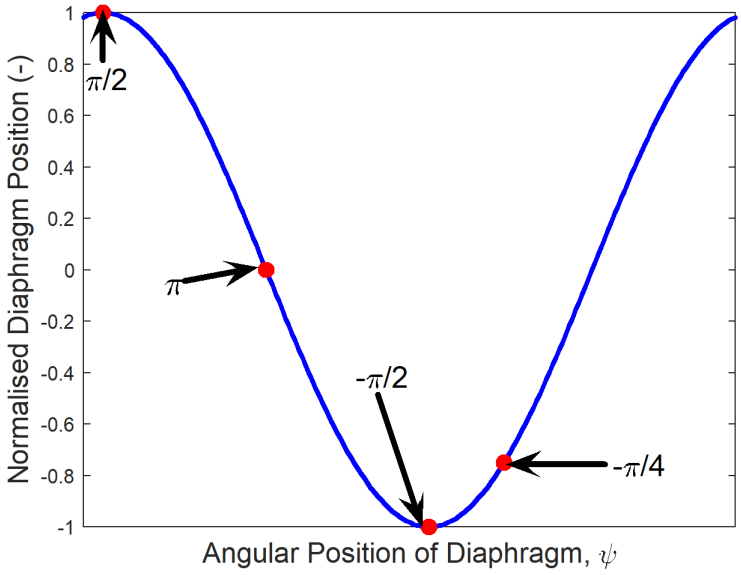

Figure 5: Diaphragm locations where flow visualizations are presented

4.1.1. Diaphragm displacement and exit jet velocity

Figure 6 presents the comparison of the model's diaphragm displacement profile with experimental data. The resonance peak at the mechanical frequency has accurately been captured around 15.9 μm, the corresponding difference between the model and experiment is 1%. The model has overestimated the displacement around the cavity acoustic resonance by 0.5 μm.

Figure 7 presents the jet velocity output comparison of the experiment and model. There is a 50 Hz difference in the model's evaluation of cavity acoustic resonance and diaphragm mechanical resonance frequencies. The peak jet velocity at both resonance frequencies is estimated within $\pm$ 2.5 ms^{-1}. Both resonance peak velocities are covered within an acceptable tolerance, and the velocity drop in the middle region between the two resonances is also captured. Table 5 summarizes the peak jet velocity output from the experiment and the model for the resonant frequencies. The velocity resolution is within 5% for the jet velocity corresponding to the mechanical resonance.

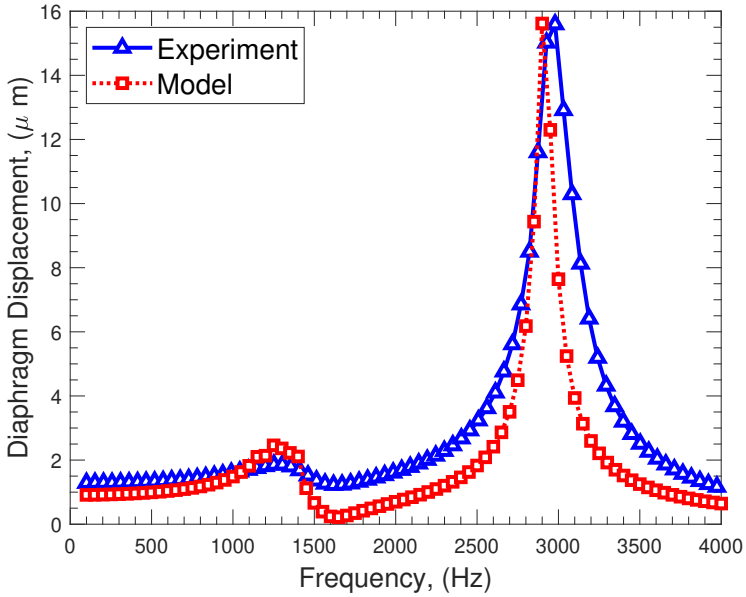

Figure 6: Case 1 - Diaphragm displacement comparison of the model and experiment

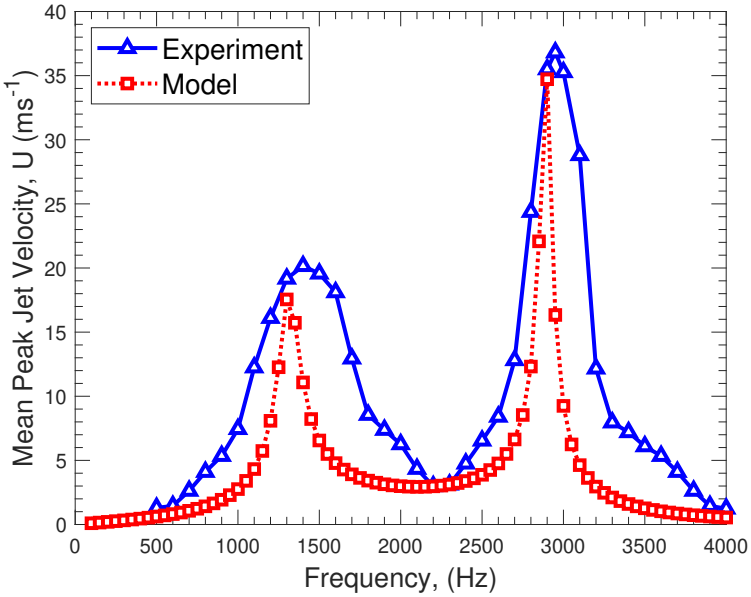

Figure 7: Case 1 - Mean peak jet velocity comparison of the model and experiment

Table 5: Validation Case 1 - Comparison of model and experiment results at resonant frequency

Resonance frequency	Helmholtz		Mechanical	
	Model	Experiment	Model	Experiment
Frequency (Hz)	1350	1400	2900	2950
Jet Velocity (ms^{-1})	17.5	20.1	34.7	36.8

Table 6 demonstrates the key non-dimensional parameters which govern the flow, such as the Stokes number (S), normalized stroke length (L), Reynolds number, based on the peak exit jet velocity (Re_{U_p}), and Strouhal number (St). The definitions and formulation of the non-dimensional numbers are consistent with the previous studies [9, 41, 42].

Table 6: Validation Case 1 - Key non-dimensional flow parameters at the mechanical resonance frequency

Parameter	Experiment	Model
S	41.7	42.0
L	1.67	1.78
Re_{U_p}	926	1002
St	1.88	1.76

4.1.2. Transient Response and Phase Relationships

The transient response of the actuator is studied to identify locations in which the flow visualizations are to be obtained. The results are presented for two frequencies corresponding to the cavity acoustic resonance and diaphragm mechanical resonance. Figure 8 presents the normalized transient data of jet velocity, in-cavity pressure, diaphragm displacement, and diaphragm velocity. It can be observed that there is a phase angle difference (ϕ) between the variables for both actuation frequencies.

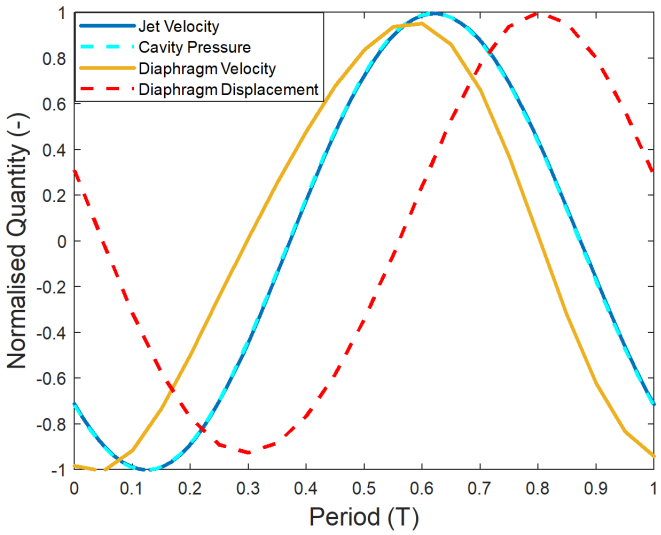

(a) $f_H = 1350$ Hz

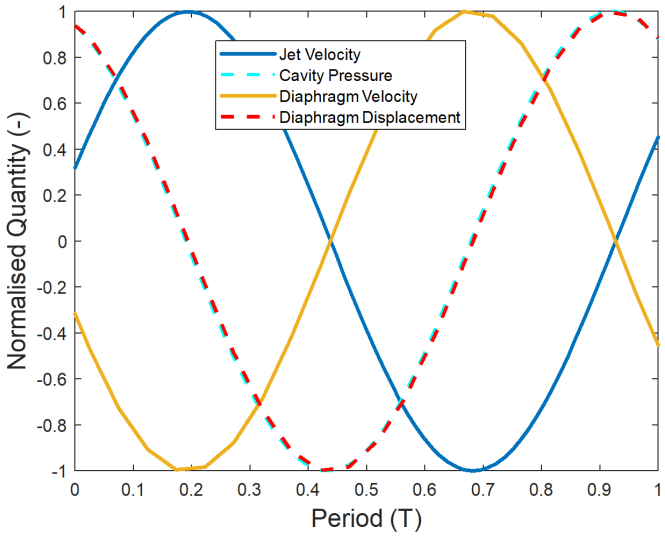

(b) $f_M = 2900$ Hz

Figure 8: Normalised transient response of key variables

Compressibility of the air in the orifice cavity originates from the exact solutions of Navier-Stokes equations of channel flow with an oscillating pressure gradient which implies a phase difference between the pressure and velocity

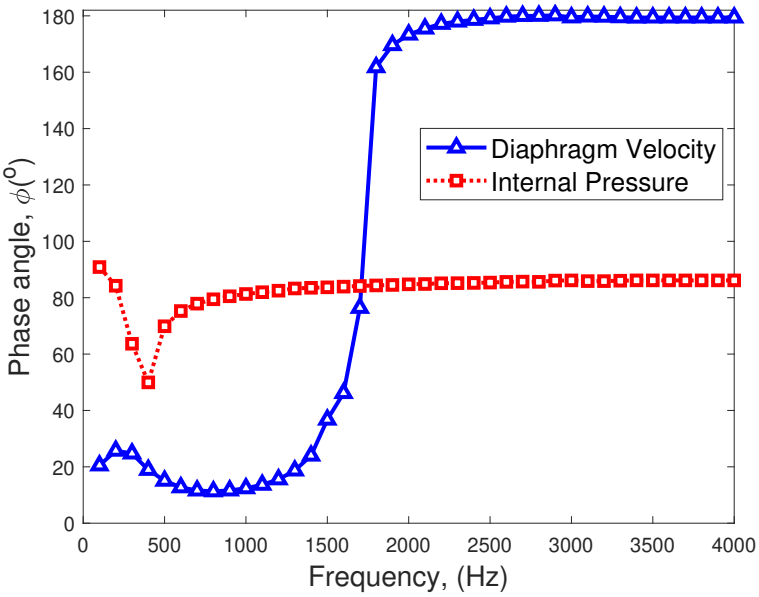

Figure 9: Validation Case 1 - Phase angle relationships

[43]. The compressibility effect results in non-linear fluid dynamic losses, thus reducing the exit jet velocity [44]. The phase relationships are studied to get further information regarding the compressibility effects from the data. The phase difference between the diaphragm and jet velocity at the orifice exit is studied. Also, the phase difference between the cavity pressure and the jet velocity at the orifice exit is investigated. Figure 9 presents the phase angle relationships between the jet velocity at the orifice and diaphragm velocity, and orifice jet velocity and internal cavity pressure.

As per the computations of Sharma [24], it is observed that the orifice jet velocity and diaphragm velocity are not in the phase when the actuation frequency is greater than the Helmholtz resonance frequency. Above the Helmholtz resonance (at 1350 Hz), the phase angle increase starts from around 1500 Hz. The phase between the diaphragm motion and jet motion becomes nearly anti-phase (reaching around 180^o), until the end of the actuation frequency range. The phase angle starts to increase at the Helmholtz resonance, and this implies that the flow is compressible for $f > f_H$. Thus, the flow becomes compressible

for actuation frequencies larger than cavity acoustic resonance.

Also, similar to the computation in [24] for the opposite diaphragm-orifice case, the orifice jet velocity and internal pressure are nearly constant, around 90^o for most of the actuation frequency range. Referring back to Figure 8b, the diaphragm and orifice exit jet velocity are in anti-phase to each other.

4.1.3. Velocity Contours

One of the key features in the simulation is linked with the visualization of the velocity and vorticity fields to demonstrate the magnitude of the jet velocity after the detachment from the orifice. It is important to quantify the formation of the jet and vorticity at the diaphragm mechanical resonance frequency as many studies only looked at the low actuation frequencies, around or smaller than Helmholtz frequency [18, 19, 20]. The flow visualizations are presented when the SJA is excited at the mechanical resonance frequency of the diaphragm; therefore, the flow compressibility is thought to be effective, which increases the pressure loss and hence reduces the exit jet velocity.

Figure 10 shows velocity contours as per the diaphragm locations shown in Figure 5 at the diaphragm mechanical resonance frequency of 2900 Hz. Figure 10a shows two jet pockets in the cavity and roll up at the orifice neck edges. Figure 10b presents the jet formation and advection away from the orifice, which reduces with the distance from the orifice. Figure 10c shows a velocity contour during the peak of the expulsion cycle, as the diaphragm and jet are out-of-phase to each other. The expulsion cycle is important to present as it proves jet formation; the jet is not sucked back into the orifice/cavity and advected in space. The large jet pocket is visible around $3\times d_o$ away from the orifice exit in which the non-dimensional stroke length, L, is 1.78. Figure 10d shows the start of the re-formation of the jet in the cavity.

4.1.4. Vorticity Contours

Vorticity contours help develop an understanding of the vortex formation in the cavity, orifice neck, and outside of the orifice. The specific importance of

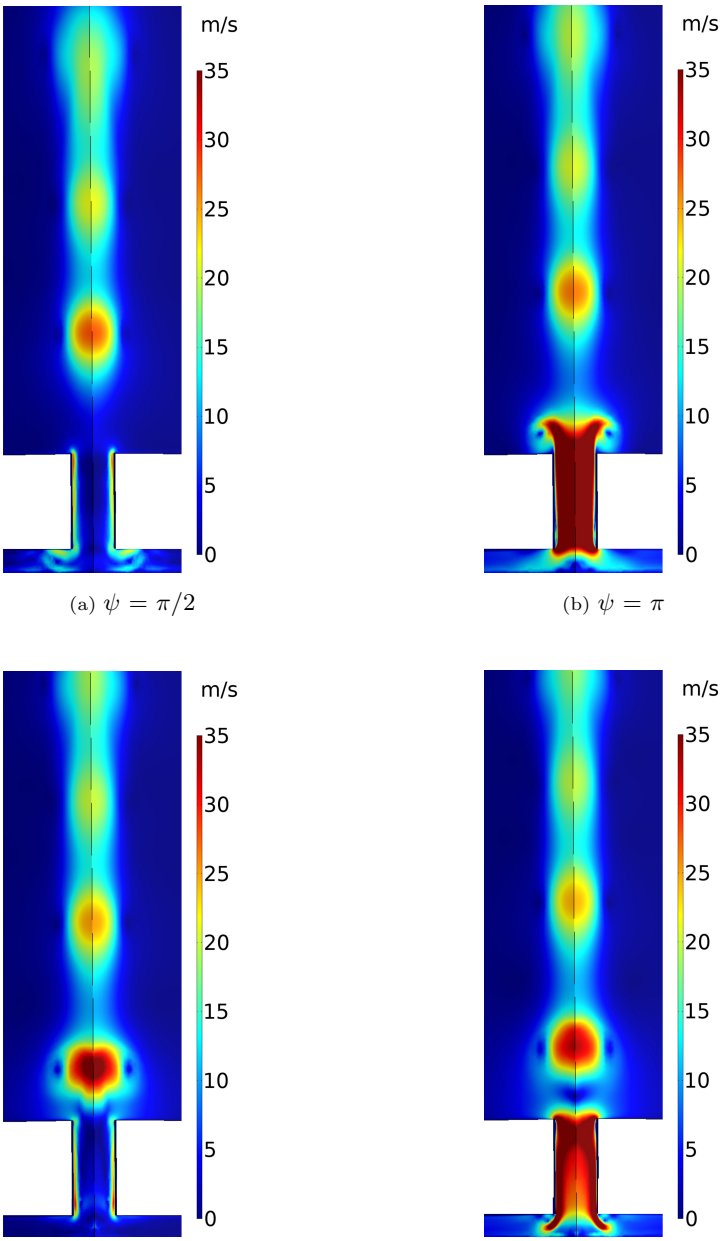

(a) $\psi = \pi/2$ (b) $\psi = \pi$

(c) $\psi = \text{-}\pi/2$ (d) $\psi = -\pi/4$

Figure 10: Numerical solutions for the validation Case 1 - Velocity Contours

this actuator is its shallow cavity employed where the viscous effects are more dominant than a larger cavity height. The frequency of actuation is 2900 Hz which coincides with the mechanical resonance of the piezoelectric diaphragm.

Figure 11 presents the vorticity contours with respect to the diaphragm locations presented in Figure 5. Figure 11a shows the ejection cycle with respect to the orifice jet velocity. The initial vortex roll-up inside the cavity is captured. At the bottom of the orifice neck, the vortex roll-up is visible. At the top of the orifice neck, vorticity strength is increased, implying the formation to take place.

Figure 11b presents the formation and advection of anti-clockwise spinning vortices where the vorticity in the bottom orifice neck is still significant. Due to the diaphragm's instantaneous neutral position, the vortices' spin is affected by their own inertia, as there is no net momentum transfer from the diaphragm to the flow.

Figure 11c shows the peak instantaneous ejection of the diaphragm. The formed vortex rings advected around $1\times d_o$ away from the orifice exit and spaced around $1.2\times d_o$ in the lateral direction. Small vortex ring formation is visible at both the top and lower edge of the orifice neck. Outer fluid is ingested back into the orifice neck, causing the separation at the orifice neck.

Figure 11d shows the start of the re-formation of the vortex rings at the cavity and the advected vorticity with reduced strength at around $1.5\times d_o$. A recirculation zone in the cavity is inspected due to the viscous fluid-structure interaction between the diaphragm and air. Also, it is shown that the vorticity is not sucked back into the cavity proving vortex formation.

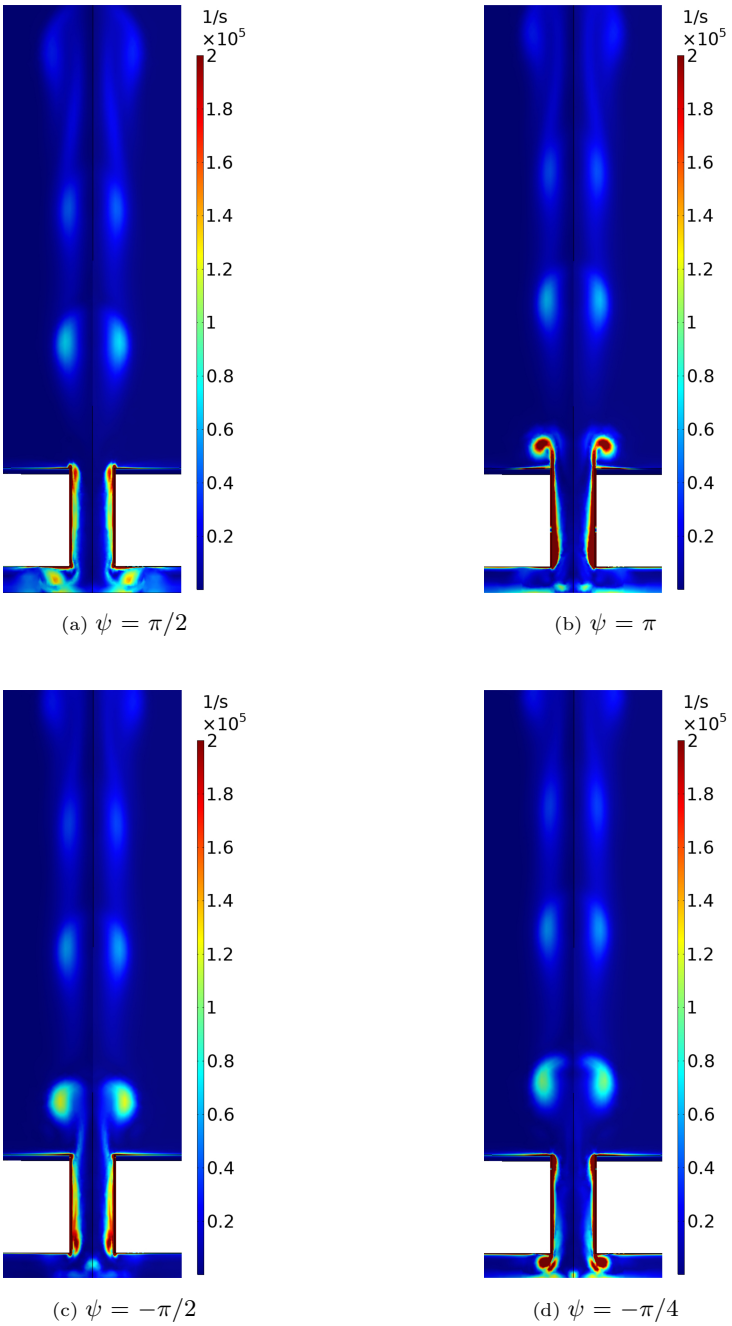

(a) $\psi = \pi/2$ (b) $\psi = \pi$

(c) $\psi = -\pi/2$ (d) $\psi = -\pi/4$

Figure 11: Numerical solutions for validation Case 1 - Vorticity Contours

4.2. Validation Case 2

This validation case investigates an adjacent SJA. The composition of the actuator geometry is presented in Figure 3b. The piezoelectric diaphragm used for Validation Case 1 is employed for this case with different cavity height and orifice diameter, as presented in Table 7. A design constraint of the adjacent orifice-diaphragm configuration is $d_o < H$. The cavity volume of validation Cases 1 and 2 are significantly different from each other, 328 mm^3 and 589 mm^3, respectively. Therefore, a direct comparison of the validation cases is not viable.

Table 7: Validation Case 2 - Cavity and orifice dimensions

Parameter	**Value**
d_o (mm)	1.0
D_c (mm)	25
h (mm)	2.5
H (mm)	1.2

4.2.1. Diaphragm displacement and exit jet velocity

Figure 12 compares the experimental peak center displacement with the model. The model matches the experiment both in resonance frequency and displacement amplitude. The response of the experiment is more damped and underestimated the magnitude for the low frequency range (i.e., 100-2500 Hz).

Figure 13 shows the comparison between the model jet velocity computation with the experimental data. The jet velocity corresponding to the mechanical resonance was identified accurately with a difference of 0.1 ms^{-1}. However, the jet velocity corresponding to the cavity acoustic resonance is underestimated by 5.1 ms^{-1}. This is due to the underestimation of diaphragm displacement at the associated frequency band. Table 8 summarizes the peak resonance response for the model and experiment. The mechanical resonance matches the experimental value both in terms of the actuation frequency and jet velocity.

Table 9 demonstrates the key non-dimensional parameters which govern the

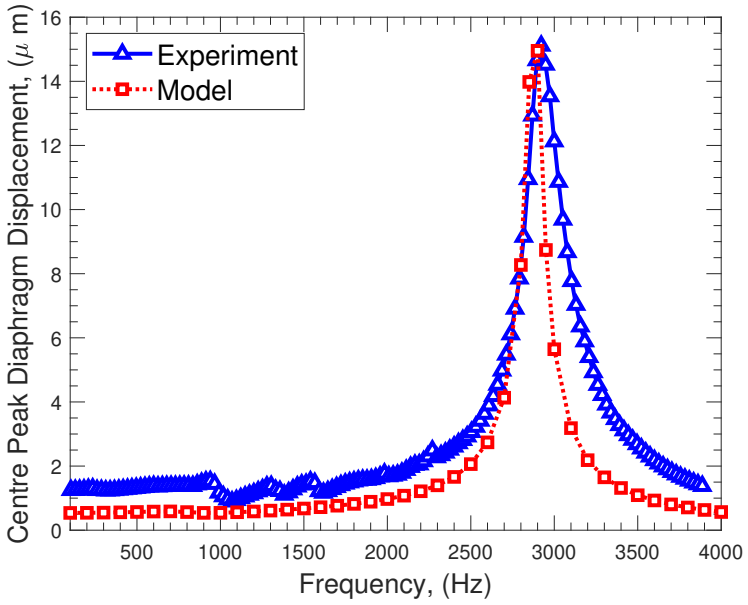

Figure 12: Case 2 - Diaphragm displacement comparison of the model and experiment

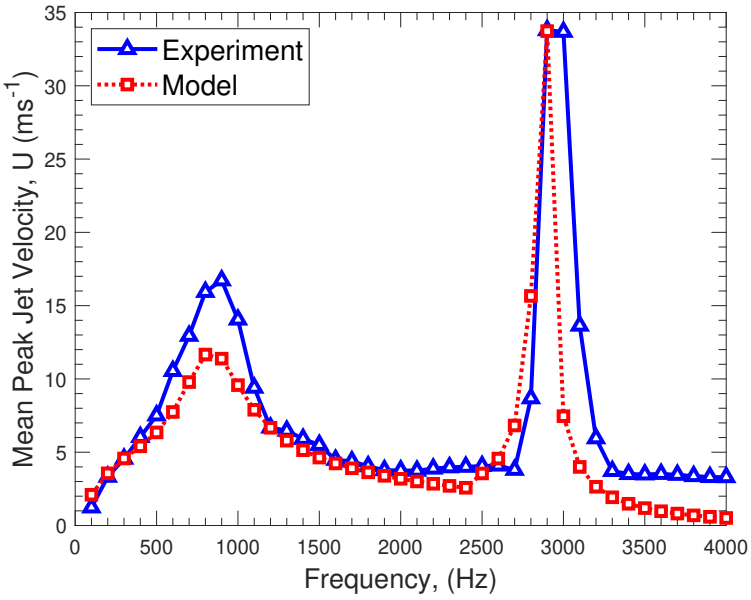

Figure 13: Case 2 - Mean peak jet velocity comparison of the model and experiment

Table 8: Validation Case 2 - Comparison of model and experiment results at resonant frequency

Resonance frequency	Helmholtz		Mechanical	
	Model	Experiment	Model	Experiment
Frequency (Hz)	800	900	2900	2900
Jet Velocity (ms^{-1})	11.6	16.7	33.7	33.8

flow, such as the Stokes number (S), normalized stroke length (L), Reynolds number based on the peak exit jet velocity (Re_{U_p}), and Strouhal number (St).

Table 9: Validation Case 2 - Key non-dimensional flow parameters at the mechanical resonance frequency

Parameter	Experiment	Model
S	34.7	34.7
L	1.35	1.33
Re_{U_p}	516	509
St	2.33	2.37

4.2.2. Transient Response and Phase Relationships

This section's structure and rationale are similar to Section 4.1.2 and concentrate on the adjacent synthetic jet. The phase relations are computed based on the diaphragm and jet velocity, and internal cavity pressure, and jet velocity.

The results are presented for two frequencies corresponding to the cavity acoustic resonance and diaphragm mechanical resonance. Figure 14 presents the normalized transient data of jet velocity, in-cavity pressure, diaphragm displacement, and diaphragm velocity. It can be observed that there is a phase lag between the variables for both actuation frequencies.

The phase relationships between the diaphragm's velocity and jet velocity are also studied for this case. Figure 15 shows the results for the phase relationships

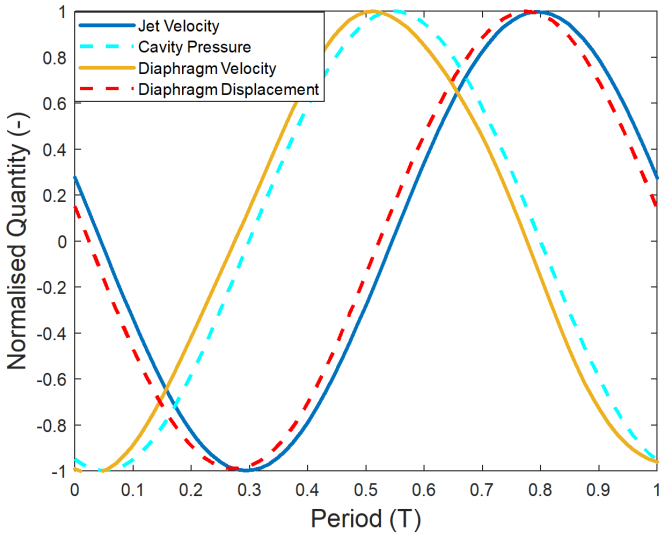

(a) f_H = 800 Hz

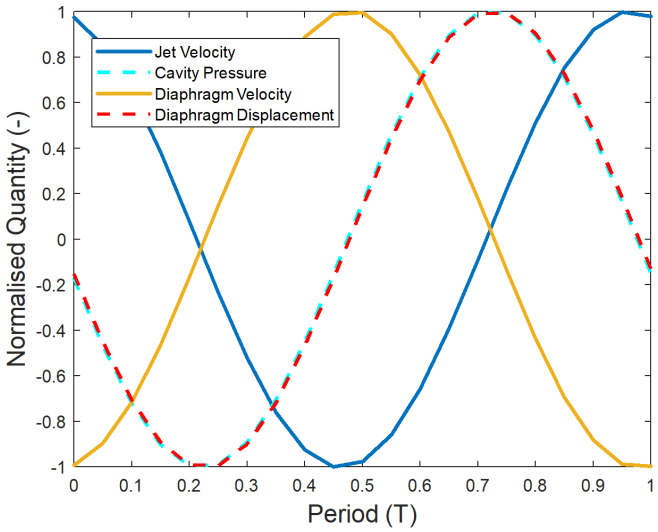

(b) f_M = 2900 Hz

Figure 14: Normalised transient response of key variables

based on the orifice exit velocity and diaphragm velocity, and also with respect to cavity internal pressure.

Orifice jet velocity and diaphragm velocity tend to have an increasing phase

angle as the actuation frequency increases and become nearly anti-phase (180^o) around 1300 Hz. At the Helmholtz resonance frequency, the phase is around 110^o. The Helmholtz resonance is at 800 Hz, which implies compressible flow after the Helmholtz resonance frequency. The orifice velocity and internal cavity pressure phase starts around 45^o and tends to be around 80^o as actuation frequency increases, which is a similar pattern compared to the opposite SJA.

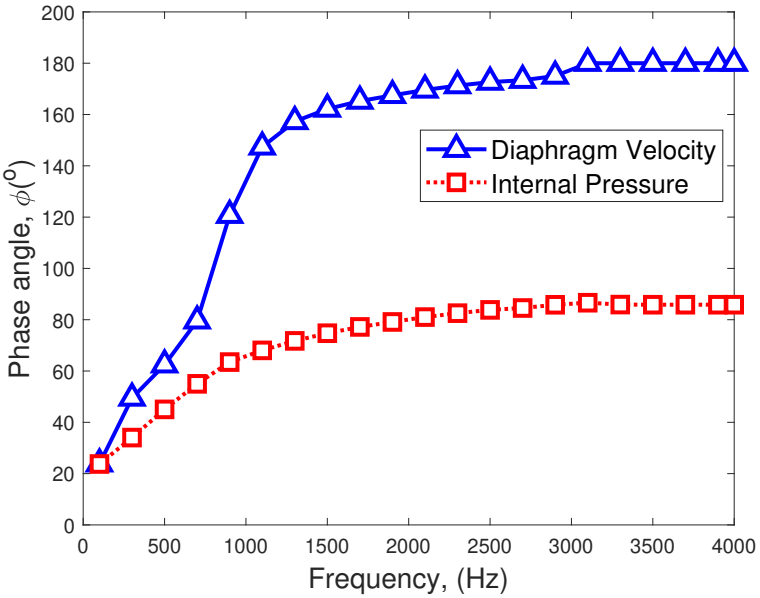

Figure 15: Case 2 - Phase angle relationships

4.2.3. Velocity Contours

The flow visualization locations of the diaphragm are identical to the validation Case 1 (see Figure 5). All figures are plotted with the same legend scale to point out the differences. Also, the same scale has been used in Figure 10. The frequency of actuation is 2900 Hz which coincides with the mechanical resonance of the piezoelectric diaphragm. Figure 16a presents the maximum instantaneous expulsion, where the diaphragm is totally out of phase with respect to the cavity. An advected jet pocket with reduced velocity is visible at $1.5\times d_o$. However, some of the fluid started to get ingested back into the cavity.

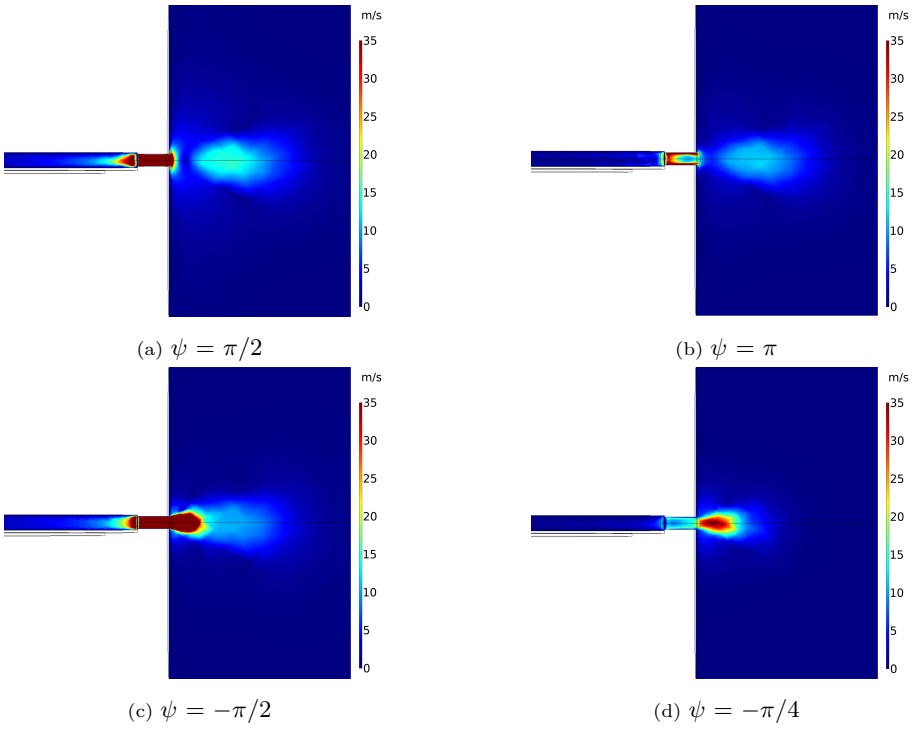

(a) $\psi = \pi/2$ (b) $\psi = \pi$

(c) $\psi = -\pi/2$ (d) $\psi = -\pi/4$

Figure 16: Numerical solutions for the validation Case 2 - velocity contours

Figure 16b shows a relatively high velocity at the orifice neck walls and lower velocity at the orifice exit due to the neutral position of the diaphragm. Instantly, the diaphragm does not energize the flow, and a low velocity is ejected out of the orifice. Flow separation is observed at the orifice neck towards the outer domain.

Figure 16c presents the maximum expulsion cycle as the diaphragm and orifice are out-of-phase with respect to each other. A dominant expulsion is observed with the disappeared separation at the orifice neck due to the high energy forcing of the flow. The jet velocity gradually decreases after $1\times d_o$. Velocity increase from the cavity to the orifice neck is visible in the cavity.

Figure 16d shows the advection of the jet, which is spread around $2\times d_0$ from the orifice exit plane. Due to the diaphragm's position, the jet flow's overall momentum is reduced.

4.2.4. Vorticity Contours

Vorticity plots of the adjacent configuration SJA are investigated from Figure 17 to detect the potential vortex formation in the cavity, orifice neck, and outer domain. Figure 17 shows only a quarter of the cavity (and also the outer domain), demonstrating a magnified view of the vortex formation region. Diaphragm motion is consistent with the previous plots and shown in Figure 5. For better visualization, the legend scale is set to be half of Figure 11. The frequency of actuation is 2900 Hz, which is the mechanical resonance of the diaphragm.

The calculated Stokes number and the non-dimensional stroke length are sufficient for the roll-up outside the orifice neck [45]. However, the vorticity field in the cavity is negligible except for the proximity of the cavity-orifice neck connection.

Figure 17a represents the bottom-most position for the ingestion and shows the vorticity entrainment within the cavity and separation in the orifice neck. The geometric contraction identifies small re-circulatory zones at the cavity-orifice neck connection.

Figure 17b shows the vorticity field where the diaphragm is instantaneously neutral. The vorticity at the orifice is further reduced due to the momentum loss of the flow.

Figure 17c shows the maximum expulsion of the orifice with two vortex rings appearing at the orifice exit. The vortex strength persisted for nearly $1.2\times$ d_o away from the orifice exit. The vortex rings are engaged at $1\times d_o$ out of orifice due to the inertial and viscous losses as the fluid en-trains. The counter-rotating vortex formation outside the orifice is a known pattern for the opposite configuration that is also valid for the adjacent design.

Figure 17d shows the reduced vorticity strength at the outer domain and at the orifice neck due to the diaphragm position, which starts ingesting the vortex field again.

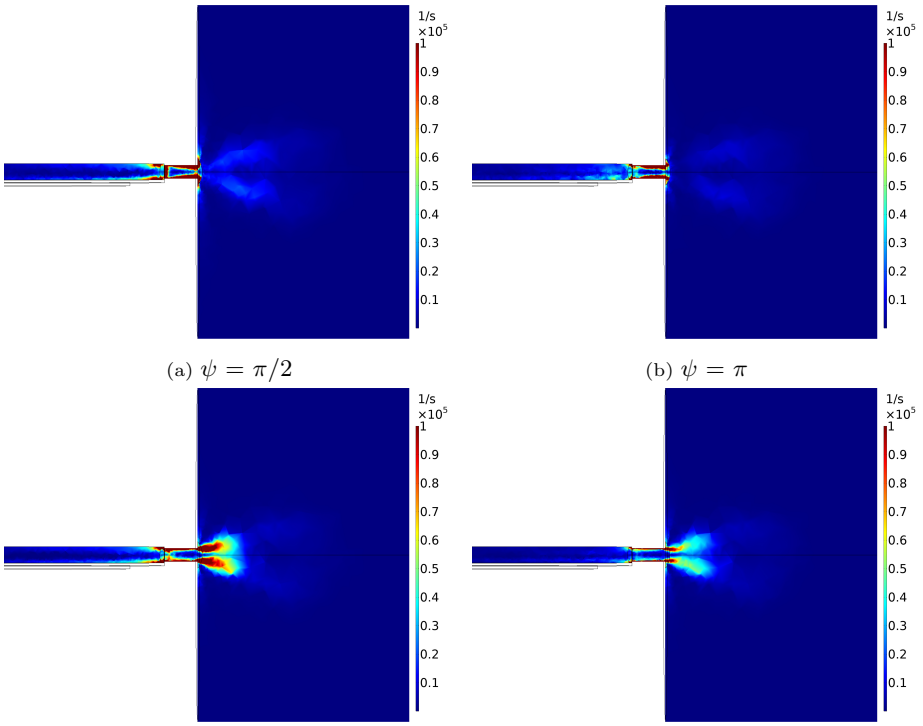

(a) $\psi = \pi/2$ (b) $\psi = \pi$

(c) $\psi = -\pi/2$ (d) $\psi = -\pi/4$

Figure 17: Numerical solutions for the validation Case 2 - vorticity contours

5. Discussion

The structural-fluidic-acoustic model presented involves modelling the piezoelectric diaphragm, which inputs pressure load (i.e., pressure fluctuations due to the motion of the diaphragm) to the cavity-orifice arrangement modelled with acoustic pressure equations. Both opposite and adjacent configuration SJAs are studied in the validation cases to take advantage of the computational model. Another important feature of the present model is the flow visualization used to obtain contour plots of jet velocity and vorticity field.

Phase difference relations are also studied by the model, which revealed that the adjacent configuration SJA tends to become compressible after the Helmholtz resonance frequency earlier than the opposite configuration. The adjacent configuration's phase angle change reaches anti-phase (180^o) more rapidly. Over the forcing frequency range, the effects of flow compressibility are more significant in an adjacent configuration actuator when compared to the opposite configuration, at which the compressibility is observed on an earlier frequency offset. This implies that compressible flow solvers should be used in a CFD study.

On the other hand, the literature is ambiguous regarding the actuation frequency (f), in which compressibility effects become significant. Gallas [46] claimed compressibility effects are important when the actuation frequency is greater than $0.5\times f_H$, whereas Sharma suggested $f > f_H$ [24]. Based on the results obtained by the multiphysics simulation, the flow starts becoming compressible when $f \approx f_H$ (initiates significant phase difference) and becomes fully compressible (i.e., diaphragm velocity and exit jet velocity are out-of-phase to each other) when $f > f_H$.

At the mechanical resonance frequency, it is found that for both Validation Cases 1 and 2, the Stokes number and non-dimensional stroke length are sufficient for vortex roll-up [45]. Vorticity contours are studied, showing evidence of the vortex formation within the cavity for the opposite configuration SJA.

In the adjacent configuration SJA case (i.e., Validation Case 2), vortex roll-

up is visible in between the cavity and orifice-neck junction. However, vortex ring formation in the cavity is not observed. Two counter-rotating vortex appearance is documented at the orifice exit. Even though the adjacent synthetic jet actuator is more suitable for an array, a significant reduction in the vortex strength is observed in this case. Thus, the vortex strength should be studied to potentially apply adjacent configuration SJA in arrays. In this case, the Stokes number is relatively large; however, in an engineering application, the orifice diameter will be likely reduced, causing the Stokes number also to reduce, which may result in no vortex roll-up. Therefore, both exit jet velocity and vortex formation/strength should be considered for development towards an engineering application.

6. Conclusions

A numerical study with extensive experimental validation has been conducted to model piezoelectric diaphragm-driven synthetic jet actuators, which can reflect their true physics of operation. The coupling between the structural mechanics and acoustics of the SJA allowed the modelling of the full actuation frequency envelope of the SJA, including cavity-acoustic and diaphragm mechanical resonance. Thus, the main shortcoming of the existing CFD models in the literature is resolved by replacing boundary conditions mimicking the piezoelectric diaphragm's motion and coupling it with acoustics.

The coupled structural-fluidic-acoustic model utilizes a multiphysics approach, proving effective diaphragm displacement and jet velocity results in two validation cases, Case 1 and Case 2 which opposite and adjacent configuration SJA has been studied, respectively. While providing an acceptable match for both validation cases, slight shifts ($\pm$100 Hz) in resonance frequency computations observed. The percentage difference between the model's jet velocity and the experiment at the mechanical resonance is 5.4% and 0.3% for cases 1 and 2, respectively. For the Helmholtz resonance jet velocity, the percentage difference is 12.9% and 30.5% for validation Cases 1 and 2, respectively.

The Helmholtz frequency of the adjacent orifice-diaphragm configuration (validation Case 2) is underestimated by 100 Hz. The jet velocity corresponding to the Helmholtz resonance is also underestimated by 5.1 ms^{-1}. Nevertheless, the mechanical resonance frequency is identified accurately, and the jet velocity matches the experimental value with a difference of 0.3%. The jet velocity peaks are predicted with a narrower band compared to the experimental data. This is thought to be due to the damping handling of the model and should be studied further to investigate the narrow-band obtained for the resonant peaks.

The computational model was used to obtain flow visualization for velocity and vorticity. Vortex formation in the cavity is observed for the opposite diaphragm-orifice configuration, unlike in the adjacent configuration. This implies that the opposite configuration's near and far-field vortex strength is higher than the adjacent configuration. Therefore, the opposite synthetic jet actuator is more likely to grant effectiveness for a potential flow control application. Also, it is found that the phase difference angle between the diaphragm's velocity and the orifice jet velocity is more dominant for the adjacent configuration.

From a practical point of view, the actuator would run at the resonant frequency in a potential engineering application; thus, estimating the resonant frequency and the corresponding jet velocity is the most critical consideration. The computational model has covered the mechanical resonance jet velocity within $\pm$ 3% difference (maximum of 2.1 ms^{-1}) for both validation cases.

References

[1] J. L. Gilarranz, L. W. Traub, O. K. Rediniotis, Characterization of a compact, high- power synthetic jet actuator for flow separation control, Aiaa 2002-0127 (2002) 1–28.

[2] J. M. Shuster, D. R. Smith, Experimental study of the formation and scaling of a round synthetic jet, Physics of Fluids 19 (2007) 1–21. doi:10.1063/1.2711481.

[3] C. S. Greco, A. Ianiro, T. Astarita, G. Cardone, On the near field of single and twin circular synthetic air jets, International Journal of Heat and Fluid Flow 44 (2013) 41–52. doi:10.1016/j.ijheatfluidflow.2013.03.018.
URL http://dx.doi.org/10.1016/j.ijheatfluidflow.2013.03.018

[4] J. Kordík, Z. Trávníček, V. Timchenko, N. A. Ismail, The predominant effect of stroke length on velocity profiles at the exit of axisymmetric synthetic jet actuators, International Journal of Heat and Fluid Flow 66 (2017) 197–208. doi:10.1016/j.ijheatfluidflow.2017.06.004.

[5] B. Gungordu, M. Jabbal, A. A. Popov, Enhancing jet velocity and power conversion efficiency of piezoelectric synthetic jet actuators, AIAA Journal (2023) 1–11doi:10.2514/1.J062930.
URL https://arc.aiaa.org/doi/10.2514/1.J062930

[6] M. Jabbal, J. Jeyalingam, Towards the noise reduction of piezoelectrical-driven synthetic jet actuators, Sensors and Actuators, A: Physical 266 (2017) 273–284. doi:10.1016/j.sna.2017.09.036.
URL https://doi.org/10.1016/j.sna.2017.09.036

[7] A. Glezer, Fluidic-based virtual aerosurface shaping, Enhancement of NATO Military Flight Vehicle Performance by Management of Interacting Boundary Layer Transition and Separation (2004) 4–7.
URL http://oai.dtic.mil/oai/oai?verb=getRecord&metadataPrefix=html&identifier=ADA442182

[8] V. Timchenko, J. Reizes, E. Leonardi, G. D. V. Davis, A criterion for the formation of micro synthetic jets, American Society of Mechanical Engineers, Fluids Engineering Division (Publication) FED 260 (2004) 197–203. doi:10.1115/IMECE2004-61374.

[9] R. Holman, Y. Utturkar, R. Mittal, B. L. Smith, L. Cattafesta, Formation criterion for synthetic jets, AIAA Journal 43 (2005) 2110–2116. doi:10.2514/1.12033.
URL http://arc.aiaa.org/doi/10.2514/1.12033

[10] D. K. L. Wu, M. A. Leschziner, Large-eddy simulations of circular synthetic jets in quiescent surroundings and in turbulent cross-flow, International Journal of Heat and Fluid Flow 30 (2009) 421–434. doi:10.1016/j.ijheatfluidflow.2009.01.007.
URL http://dx.doi.org/10.1016/j.ijheatfluidflow.2009.01.007

[11] M. Ja'Fari, A. J. Jaworski, A. Rona, Numerical study of flow separation control over a circular hump using synthetic jet actuators, AIP Advances 12 (2022). doi:10.1063/5.0099926.
URL https://doi.org/10.1063/5.0099926

[12] D. R. Smith, Interaction of a synthetic jet with a crosss ow boundary layer, Aiaa Journal 40 (2002). doi:10.2514/2.1564.

[13] M. B. Chiekh, J. C. Béra, M. Sunyach, Synthetic jet control for flows in a diffuser: Vectoring, spreading and mixing enhancement, Journal of Turbulence 4 (2003) 1–12. doi:10.1088/1468-5248/4/1/032.

[14] Y. Kang, Z. bing Luo, X. Deng, P. Cheng, C. Peng, W. He, Z. xun Xia, Numerical study of a liquid cooling device based on dual synthetic jets actuator, Applied Thermal Engineering 219 (2023) 119691. doi:10.1016/j.applthermaleng.2022.119691.
URL https://doi.org/10.1016/j.applthermaleng.2022.119691

[15] J. L. Gilarranz, L. W. Traub, O. K. Rediniotis, A new class of synthetic jet actuators—part ii: Application to flow separation control, Journal of Fluids Engineering 127 (2005) 377. doi:10.1115/1.1882393.
URL http://fluidsengineering.asmedigitalcollection.asme.org/article.aspx?articleid=1430147

[16] P. Itsariyapinyo, R. N. Sharma, Experimental study of a naca0015 circulation control airfoil using synthetic jet actuation, AIAA Journal 60 (2022) 1612–1629. doi:10.2514/1.J060508.
URL https://doi.org/10.2514/1.J060508

[17] L. D. Kral, J. Donovan, A. Cain, A. Cary, Numerical simulation of synthetic jet actuators, Aiaa 97-1824 (1997) 14.

[18] M. Jain, B. Puranik, A. Agrawal, A numerical investigation of effects of cavity and orifice parameters on the characteristics of a synthetic jet flow, Sensors and Actuators, A: Physical 165 (2011) 351–366. doi:10.1016/j.sna.2010.11.001.
URL http://dx.doi.org/10.1016/j.sna.2010.11.001

[19] S. Alimohammadi, E. Fanning, T. Persoons, D. B. Murray, Characterization of flow vectoring phenomenon in adjacent synthetic jets using cfd and piv, Computers and Fluids 140 (2016) 232–246. doi:10.1016/j.compfluid.2016.09.022.

[20] P. Ziadé, M. A. Feero, P. E. Sullivan, A numerical study on the influence of cavity shape on synthetic jet performance, International Journal of Heat and Fluid Flow 74 (2018) 187–197. doi:10.1016/j.ijheatfluidflow.2018.10.001.
URL https://doi.org/10.1016/j.ijheatfluidflow.2018.10.001

[21] Q. Gallas, R. Holman, T. Nishida, B. Carroll, M. Sheplak, L. Cattafesta, Lumped element modeling of piezoelectric-driven synthetic jet actuators, AIAA Journal 41 (2003) 240–247. doi:10.2514/2.1936.
URL http://arc.aiaa.org/doi/10.2514/2.1936

[22] H. Tang, S. Zhong, Lumped element modelling of synthetic jet actuators, Aerospace Science and Technology 13 (2009) 331–339. doi:10.1016/j.ast.2009.06.004.
URL http://dx.doi.org/10.1016/j.ast.2009.06.004

[23] T. Persoons, General reduced-order model to design and operate synthetic jet actuators, AIAA Journal 50 (2012) 916–927. doi:10.2514/1.J051381.

[24] R. N. Sharma, Fluid dynamics-based analytical model for synthetic jet

actuation, AIAA Journal 45 (2007) 1841–1847. doi:10.2514/1.25427.
URL http://arc.aiaa.org/doi/10.2514/1.25427

[25] T. Persoons, T. S. O'Donovan, A pressure-based estimate of synthetic jet velocity, Physics of Fluids 19 (2007) 4–7. doi:10.1063/1.2823560.

[26] H. Tang, S. Zhong, A static compressible flow model of synthetic jet actuators, Aeronautical Journal 111 (2007) 421–431. doi:10.1017/S0001924000004681.

[27] M. Chiatto, F. Capuano, G. Coppola, L. D. Luca, Lem characterization of synthetic jet actuators driven by piezoelectric element: A review, Sensors (Switzerland) 17 (2017). doi:10.3390/s17061216.

[28] Q. Gallas, J. Mathew, A. Kasyap, R. Holman, T. Nishida, B. Carroll, M. Sheplak, L. Cattafesta, Lumped element modeling of piezoelectric-driven synthetic jet actuators, AIAA Journal 41 (2003) 240–247. doi:10.2514/2.1936.
URL http://arc.aiaa.org/doi/10.2514/2.1936

[29] D. P. Rizzetta, M. R. Visbal, M. J. Stanek, Numerical investigation of synthetic-jet flowfields, AIAA Journal 37 (1999) 919–927. doi:10.2514/2.811.
URL http://arc.aiaa.org/doi/10.2514/2.811

[30] S. Mallinson, J. Reizes, G. Hong, An experimental and numerical study of synthetic jet flow, Aeronautical Journal 105 (2001).

[31] H. Tang, S. Zhong, 2d numerical study of circular synthetic jets in quiescent flows, Aeronautical Journal 109 (2005) 89–97. doi:10.1017/S0001924000000592.

[32] A. Qayoum, A. Malik, Influence of the excitation frequency and orifice geometry on the fluid flow and heat transfer characteristics of synthetic jet actuators, Fluid Dynamics 54 (2019) 575–589. doi:10.1134/S0015462819040086.

[33] Comsol multiphysics acoustics module users guide (2018).
URL https://doc.comsol.com/5.4/doc/com.comsol.help.aco/AcousticsModuleUsersGuide.pdf

[34] M. Papila, M. Sheplak, L. N. Cattafesta, Optimization of clamped circular piezoelectric composite actuators, Sensors and Actuators, A: Physical 147 (2008) 310–323. doi:10.1016/j.sna.2008.05.018.

[35] P. Mane, K. Mossi, R. Bryant, Synthetic jets with piezoelectric diaphragms, Smart Structures and Materials 5761 (2005) 233. doi:10.1117/12.599584.
URL http://proceedings.spiedigitallibrary.org/proceeding.aspx?doi=10.1117/12.599584

[36] C. R. Rosas, Numerical simulation of flow separation control by oscillatory fluid injection, Texas AM University Doctoral (2003).

[37] Y. W. Lv, J. Z. Zhang, Y. Shan, X. M. Tan, Numerical investigation for effects of actuator parameters and excitation frequencies on synthetic jet fluidic characteristics, Sensors and Actuators, A: Physical 219 (2014) 100–111. doi:10.1016/j.sna.2014.08.009.

[38] H. Tang, S. Zhong, M. Jabbal, L. Garcillan, F. Guo, N. Wood, C. Warsop, Towards the design of synthetic-jet actuators for full-scale flight conditions : Part 2: Low-dimensional performance prediction models and actuator design method, Flow, Turbulence and Combustion 78 (2007) 309–329. doi:10.1007/s10494-006-9061-3.

[39] R. Oshana, Overview of digital signal processing algorithms, DSP Software Development Techniques for Embedded and Real-Time Systems (2006) 59–121doi:10.1016/B978-075067759-2/50006-5.

[40] L. Gomes, W. Crowther, Towards a practical piezoceramic diaphragm based synthetic jet actuator for high subsonic applications - effect of chamber and orifice depth on actuator peak velocity, 2006. doi:10.2514/6.

2006-2859.
URL http://arc.aiaa.org/doi/10.2514/6.2006-2859

[41] S. Zhong, M. Jabbal, H. Tang, L. Garcillan, F. Guo, N. Wood, C. Warsop, Towards the design of synthetic-jet actuators for full-scale flight conditions : Part 1: The fluid mechanics of synthetic-jet actuators, Flow, Turbulence and Combustion 78 (2007) 283–307. doi:10.1007/s10494-006-9064-0.

[42] Q. Xia, S. Lei, J. Ma, S. Zhong, Numerical study of circular synthetic jets at low reynolds numbers, International Journal of Heat and Fluid Flow 50 (2014) 456–466. doi:10.1016/j.ijheatfluidflow.2014.10.019.

[43] T. V. Buren, E. Whalen, M. Amitay, Achieving a high-speed and momentum synthetic jet actuator, Journal of Aerospace Engineering 29 (2016) 04015040. doi:10.1061/(ASCE)AS.1943-5525.0000530.
URL http://ascelibrary.org/doi/10.1061/%28ASCE%29AS.1943-5525.0000530

[44] W. J. Crowther, L. T. Gomes, An evaluation of the mass and power scaling of synthetic jet actuator flow control technology for civil transport aircraft applications, Proceedings of the Institution of Mechanical Engineers. Part I: Journal of Systems and Control Engineering 222 (2008) 357–372. doi:10.1243/09596518JSCE519.

[45] J. Zhou, H. Tang, S. Zhong, Vortex roll-up criterion for synthetic jets, AIAA Journal 47 (2009) 1252–1262. doi:10.2514/1.40602.

[46] Q. Gallas, On the modeling and design of zero-net mass flux actuators (2005).
URL https://ufdc.ufl.edu/UFE0008338/00001